JOURNAL OF SYNCHROTRON RADIATION

ISSN 1600-5775

Received 12 February 2019
Accepted 3 June 2019

Edited by K. Tiedtke, DESY, Germany

[1] This article will form part of a virtual special issue containing papers presented at the PhotonDiag2018 workshop.

Keywords: Kirkpatrick–Baez; wavefront sensor; *WISEr*; active optics system; FERMI.

Kirkpatrick–Baez active optics system at FERMI: system performance analysis[1]

Lorenzo Raimondi,[a]* Michele Manfredda,[a] Nicola Mahne,[b] Daniele Cocco,[c] Flavio Capotondi,[a] Emanuele Pedersoli,[a] Maya Kiskinova[a] and Marco Zangrando[a,b]

[a]Elettra – Sincrotrone Trieste, SS 14 km 163.5 in Area Science Park, 34149 Trieste, Italy, [b]IOM-CNR – Istituto Officina dei Materiali – Consiglio Nazionale delle Ricerche, SS 14 km 163.5 in Area Science Park, 34149 Trieste, Italy, and [c]SLAC National Accelerator Laboratory, 2575 Sand Hill Rd, MS-19, Menlo Park, CA 94025, USA. *Correspondence e-mail: lorenzo.raimondi@elettra.eu

FERMI is the first and only seeded EUV-SXR free-electron laser (FEL) facility available to users; it operates at Elettra – Sincrotrone Trieste (Italy) and it presents five operating endstations. Three of them, namely LDM (Low Density Matter), DiProI (Diffraction and Projection Imaging) and MagneDyn (Magneto-Dynamical studies), use a Kirkpatrick–Baez (KB) active X-ray optics system to focus the FEL pulses into the experimental chambers. The present work reports on the final results of the upgraded KB Active Optics Systems (KAOS), which have been mechanically modified in order to improve stability and repeatability with respect to the original design. The results have been obtained on both the FERMI FEL lines, FEL1 and FEL2, and are particularly relevant for the latter as it is the low-wavelength line recently opened to users. After a thorough description of the new mechanical layout of the system and the aspects that have been improved after the refurbishment, a set of simulations of the optical performances are presented. The code used to simulate the behavior of KAOS is *WISEr*, a physical-optics-based tool, which is freely accessible, and integrated into the Oasys platform, that takes into account the specific surface metrology characterization of the beamline mirrors, including figure errors and microroughness power spectral density. The results of *WISEr* are then used as a reference for the actual optimization of the optical system. This procedure relies heavily on a wavefront sensor (WFS) mounted out of focus to optimize the refocusing mirrors alignment as well as their curvature bending (by minimization of the coefficients of the Zernike wavefront expansion). Moreover, the WFS data are used to reconstruct the focal spot parameters by means of a back-propagation of the electric field. Finally, these results are compared with those obtained after the FEL ablation of a PMMA layer positioned on the focal plane, and analyzed *ex situ* in a post-mortem fashion. The mechanically refurbished optical system and the multi-technique alignment approach, aimed at optimizing the mirrors' curvature, pitch and roll angles, allowed a focal spot of 1.8 µm × 2.4 µm at 4.14 nm wavelength (FEL2) to be inferred, confirmed by the PMMA ablation imprints.

1. Introduction

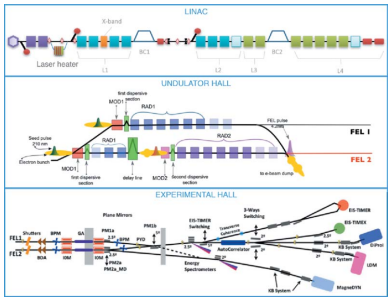

FERMI is a single-pass free-electron laser (FEL) user-facility covering in the first harmonic the wavelength range from 100 nm to 4 nm (EUV to soft X-rays). It is located next to the third-generation synchrotron radiation facility Elettra in Trieste, Italy (Allaria *et al.*, 2010, 2012, 2013; Prince *et al.*, 2016). The implemented seeded FEL scheme guarantees the generation of highly coherent (transversely and longitudinally), ultrabright pulses, and the use of APPLE II-type undulators allows for variable polarization (linear horizontal/vertical, right/left circular). The machine layout comprises two FEL lines designed to cover efficiently the wavelength range

and conceived to generate short radiation pulses ($\tau \simeq 30$–100 fs). The mentioned capabilities together with the possibility to operate FERMI also in more-exotic emission schemes (*e.g.* two-color double pulses, phase-controlled double pulses, *etc*.) have opened new experimental opportunities that were not achievable before (Allaria *et al.*, 2012).

The unique features of FERMI, together with the possibility to perform single-shot experiments thanks to the pulse ultrahigh intensity, call for a dedicated diagnostic section capable of providing photon beam information to the users. PADReS, which stands for Photon Analysis Delivery and REduction System (Zangrando *et al.*, 2011, 2015), is the section of FERMI devoted to characterize, manipulate and deliver the photon beam to the experimental endstations. PADReS provides various information such as shot-to-shot intensity, spectral distribution, beam transverse position, coherence and wavefront characterization. Intensity, spectral distribution and beam position are resolved non-invasively and pulse by pulse, while beam coherence and wavefront characterization involve invasive measurements. A gas absorber gives the user the possibility to reduce the photon beam intensity by up to four orders of magnitude. PADReS also includes filtering, splitting-delaying and focusing systems.

The five endstations already operative at FERMI are: EIS-TIMEX (di Cicco *et al.*, 2011), EIS-TIMER (Foglia *et al.*, 2017; Masciovecchio *et al.*, 2015), LDM (O'Keeffe *et al.*, 2011; Svetina *et al.*, 2015), DiProI (Pedersoli *et al.*, 2011; Capotondi *et al.*, 2015) and MagneDyn (Svetina *et al.*, 2014).

After the acceleration section, the electron bunch can be sent to two different undulator chains. The two chains generate two different sources named FEL1 and FEL2, working in two different energy ranges: FEL1 between 100 nm and 20 nm and FEL2 between 20 nm and 4 nm. Moreover, since the photon generation almost fulfills the transform limit, the beam divergence is a function of the wavelength (Allaria *et al.*, 2010). Finally, the FEL2 undulator chain is longer than the FEL1 one, as it is based on a double-cascade high-gain harmonic generation scheme, moving its effective photon source 7 m closer to the endstations than the one of FEL1 (see Fig. 1).

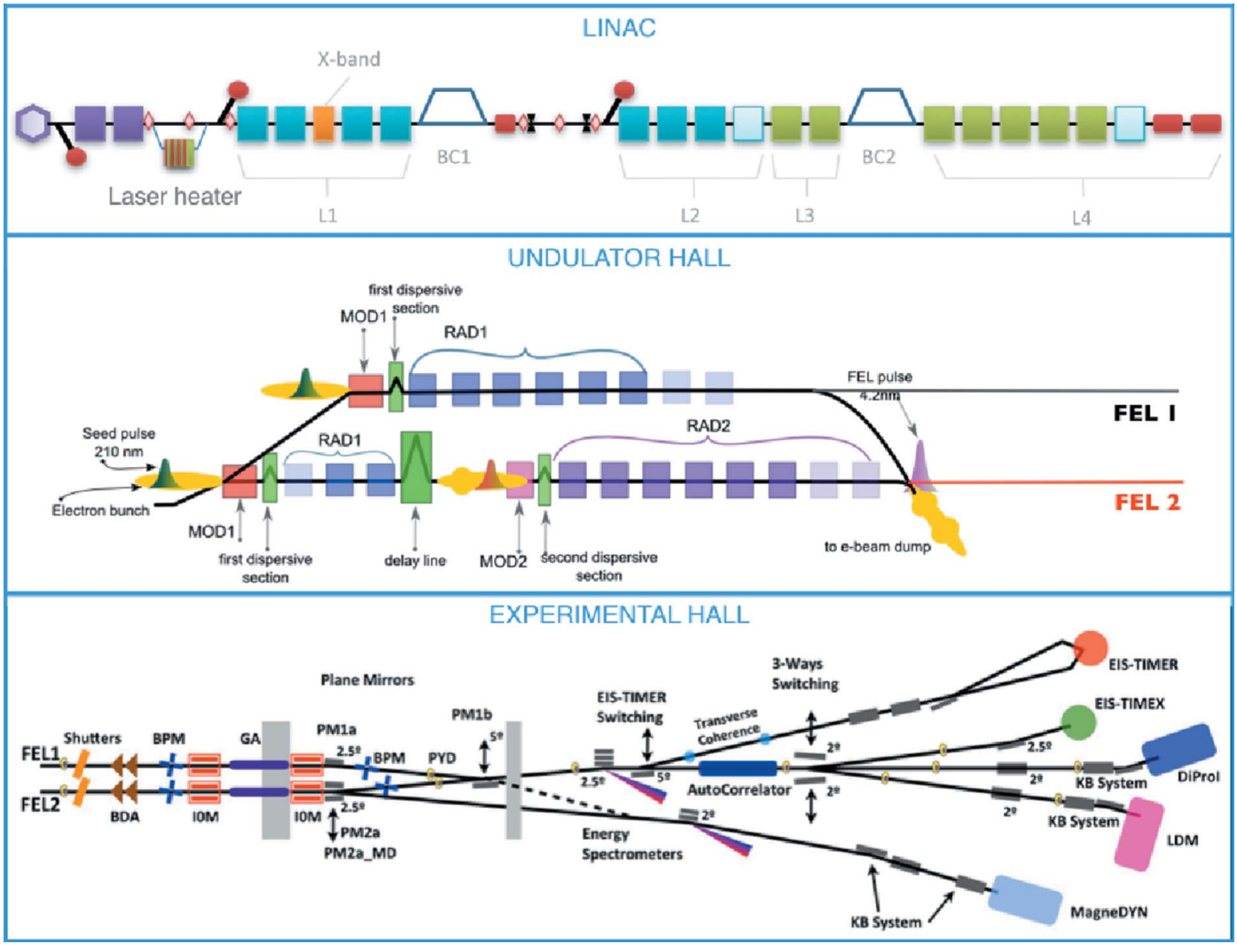

Figure 1
Layout of the three main sections of FERMI: injector and linac tunnel; the undulator hall; the experimental hall.

The general request for the experiments is to have micrometre-sized focal spots with high fluence at focus. Consequently the target of PADReS is to employ optical systems characterized by high focusing performance. The sizes of FEL1 and FEL2 photon sources in terms of σ are 124 and 59 µm, respectively (estimated at 32 nm for FEL1 and at 10 nm for FEL2), so the de-magnifications requested to the refocusing systems are quite demanding (*i.e.* typically between 50 and 100), excluding the case of the EIS-TIMER beamline. The sizes of the photon source depend on the particular optimization of the machine, from time to time may be subject to variation, and may be even dependent on the selected photon wavelength. All these constrains call for dedicated and versatile focusing systems, capable of adapting their performance to the chosen FEL line. The systems tackling such a demanding task are the Kirkpatrick–Baez (Kirkpatrick & Baez, 1948) (KB) active optics systems (KAOS), except for EIS-TIMEX and EIS-TIMER.

Each KAOS consists of a couple of plane-elliptical mirrors that can be independently bent in a controlled way by means of mechanical benders. They have several advantages: (i) they allow decoupling of vertical and horizontal beam components, (ii) they can focus two photon sources located at different distances (such as FEL1 and FEL2) using the same pair of mirrors, and (iii) they use thin plane mirrors (which are easier to manufacture with respect to bulk elliptical mirrors) mechanically bent into a plane-elliptical shape capable of dealing with the requested magnifications ($M_\mathrm{v} \times M_\mathrm{h} \simeq 60 \times 80$). Finally, with such active systems, it is in principle possible to improve the FEL beam wavefront quality by compensating the undesired astigmatisms caused by the figure errors of plane mirrors along the whole optical system.

EIS-TIMER is an FEL-based four-wave-mixing instrument, employing a complex refocusing system based on toroidal mirrors, while for EIS-TIMEX a single ellipsoidal mirror has been chosen to minimize the number of optical reflections before the sample (Masciovecchio *et al.*, 2015).

2. *WISEr* simulator

WISEr is a physical optics simulation package used to compute the complex electromagnetic field downstream of one or more optical elements. It exploits a wavefront propagation method based on physical optics implemented in 2010 (Raimondi & Spiga, 2010) and developed over the years (Raimondi *et al.*, 2013; Raimondi & Spiga, 2015). It has been recently updated and included in the Orange Synchrotron Suite (OASYS; Sanchez del Rio *et al.*, 2014), a new graphical environment that gathers most of the simulation tools developed and used within the synchrotron and free-electron laser communities. *WISEr* is specialized in operating at high-energy wavelengths (from extreme ultraviolet to hard X-rays) and grazing angles of incidence, using spatial and temporal fully coherent sources. At grazing incidence, where the reflection in the XUV range is higher, diffraction is more effective in the tangential direction than in the sagittal one, usually by a 100- to 1000-fold factor. This allows the mirror sagittal error to be neglected. We consider the case of an isotropic point-like source on the optical axis at $z = S$ of an axially symmetric, grazing-incidence mirror sector characterized by the radial profile $x_1(z_1)$. The electric field diffracted in the xz plane can be easily computed by means of the Huygens–Fresnel principle. Defining $d_2 = [(x_1 - x)^2 + (z_1 - z)^2]^{1/2}$, and S the z source coordinate, the computation of the intensity distribution in the focal plane at $z = 0$, which we will refer to as the point spread function (PSF), is thus performed using Kirchoff's scalar diffraction formula over a 1D domain,

$$\mathrm{PSF}(x) = \frac{\Delta R_1}{L_1^2 \lambda R_0} \left| \int_f^{f+L_1} \left(\frac{x_1}{\bar{d}_{2,0}} \right)^{1/2} \times \exp\left\{ -\frac{2\pi i}{\lambda} \left[\bar{d}_{2,0} - z_1 + \frac{x_1^2}{2(S - z_1)} \right] \right\} \mathrm{d}z_1 \right|^2, \quad (1)$$

where f is the nominal focal distance, $L \ll f$ is the mirror length, ΔR is the maximum − minimum radius, and λ is *any* wavelength to be focused. We thereby assume the mirror surface to be described as a rotation of a 1D profile about the z-axis, that is the radial coordinate as a function of the mirror's axial coordinate, $r = r_1(z_1)$, which in turn equals the longitudinal mirror profile in the xz plane $x_1(z_1)$. In practice, x_1 is composed of three terms as follows,

$$x_1(z_1) = x_{\mathrm{n1}}(z_1) + x_{\mathrm{meas1}}(z_1) + x_{\mathrm{PSD1}}(z_1), \quad (2)$$

where x_{n1} is the nominal mirror profile, x_{meas1} is *the* measured profile error along the entire profile length L_1, and x_{PSD1} is *one* of the infinitely possible profiles of length L_1, computed from the PSD. The latter is obtained from a roughness characterization in a broad spectral range, but not overlapping the frequency window of the instrument used to measure x_{meas1}. The reason for the different treatments for the two terms is that the resolution of x_{meas1} cannot be extended down to the typical frequencies of microroughness. In turn, instruments dedicated to roughness measurements (*i.e.* interferometers or atomic force microscopes) cannot be extended to scan lengths of more than a few millimetres. Hence, the PSD characterization can be used to obtain one of the *infinitely possible* profiles of length L_1 (Raimondi & Spiga, 2015) that are consistent with the measured roughness PSD. The reason for the profile degeneracy is in the phase information of the Fourier components of the roughness, that are lost when computing the PSD. To reconstruct the profile from the PSD, the phase of the components can be freely selected. Each choice results in a different rough profile, which *in principle* might exhibit different scattering properties.

Fortunately, one of the results of the first-order X-ray scattering theory is that the scattering pattern only depends on the PSD if the r.m.s. of x_{PSD1} fulfills the smooth surface condition (Church, 1979; Stover, 1995), *i.e.* that

$$\left(\int_0^{L_1} x_{\mathrm{PSD1}} \, \mathrm{d}z_1 \right)^{1/2} < \frac{\lambda}{4\pi \sin \alpha_1}, \quad (3)$$

where α_1 is the incident angle. Equation (3) is usually fulfilled by optically polished surfaces, so we expect the PSF contribution of $x_{\rm PSD1}$ to depend not on the particular realization of the profile but solely on the PSD.

The method can be extended easily (Raimondi & Spiga, 2015) to multiple reflections. Consider, for instance, the case of the double reflection, a couple of longitudinal profiles, and assume that the profile is described by the radial coordinate as a function of z, which in the xz plane is denoted by $x_1(z_1)$ of length L_1 for the primary, and $x_2(z_2)$ of length L_2 for the secondary (see Fig. 2). The primary mirror collects the radiation from an isotropic, point-like X-ray source at $z = S$ and diffracts it onto the secondary, which eventually diffracts the wave to a focus. The nominal focal plane is still assumed to be at $z = 0$. The corresponding radial amplitudes are, respectively, $\Delta R_1 = L_1\alpha_1$ and $\Delta R_2 = L_2\alpha_2$, where α_1 and α_2 are the incidence angles. In real cases, a profile including low-, mid- and high-frequency errors will be superposed to each ideal mirror shape. The computation now involves two steps: first, the diffracted field on the secondary mirror at the xz plane is computed using

$$E_2(x_2, z_2) = \frac{E_0\,\Delta R_1}{L_1(\lambda x_2)^{1/2}} \int_f^{f+L_1} \left(\frac{x_1}{\bar{d}_{12}}\right)^{1/2} \times \exp\left\{-\frac{2\pi i}{\lambda}\left[\bar{d}_{12} - z_1 + \frac{x_1^2}{2(S - z_1)}\right]\right\} {\rm d}z_1, \quad (4)$$

where $\bar{d}_{12}$ is the distance in the xz plane from a generic point of the primary mirror to a generic point on the secondary mirror,

$$\bar{d}_{12} = \left[(x_2 - x_1)^2 + (z_2 - z_1)^2\right]^{1/2}. \quad (5)$$

The subsequent diffraction by the secondary segment, at any position in the xz plane (in-, intra- or extra-focus), is simply obtained from the application of the equation related to the single reflection weighting its integrand on the *complex* E_2 function obtained from equation (4),

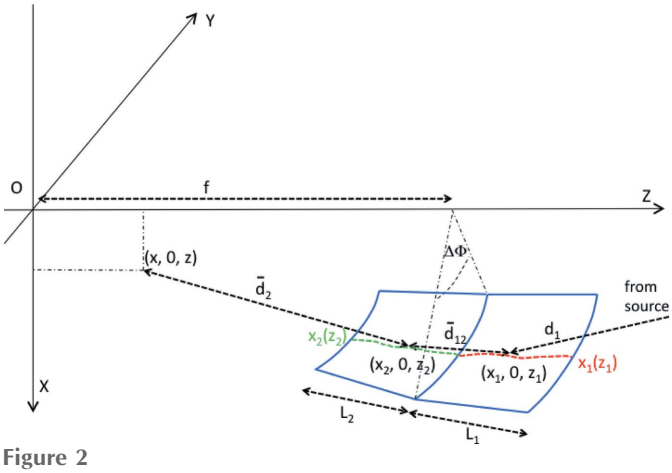

Figure 2
Scheme used for the computation of the electric field diffracted by a double reflection.

$$E(x, z) = \frac{E_0\,\Delta R_2}{L_2(\lambda x)^{1/2}} \int_{f-L_2}^{f} E_2(x_2, z_2)\left(\frac{x_2}{\bar{d}_2}\right)^{1/2} \times \exp\left(-\frac{2\pi i}{\lambda}\,\bar{d}_2\right) {\rm d}z_2. \quad (6)$$

In the last equation the complex expression of E_2 already includes all the relevant information on the phase; hence, the terms in the exponent that include the '1' subscript have been dropped off. Only the distance $\bar{d}_2$ remains therein,

$$\bar{d}_2 = \left[(x_2 - x)^2 + (z_2 - z)^2\right]^{1/2}. \quad (7)$$

Finally, the final computation of the PSF in the nominal focal plane is done taking the squared module of equation (6) at $z = 0$, and normalizing to the intensity collected within the radial aperture effective for double reflection, $\Delta R_{\rm min}$,

$${\rm PSF}_2(x) = \frac{\Delta R_{\rm min}}{E_0^2 L_2 f\lambda}\left| \int_{f-L_2}^{f} E_2(x_2, z_2)\left(\frac{x_2}{\bar{d}_{2,0}}\right)^{1/2} \times \exp\left(-\frac{2\pi i}{\lambda}\,\bar{d}_{2,0}\right) {\rm d}z_2\right|^2, \quad (8)$$

where $\bar{d}_{2,0}$ is evaluated at $z = 0$. The last expression is independent of the incident radiation intensity, and normalized to 1 when integrated over x.

The results can be easily extended to the case of an on-axis anisotropic source but at finite distance, as commonly experienced with on-ground X-ray sources [*e.g.* synchrotrons or FELs (Raimondi *et al.*, 2013)], and to an arbitrary number of reflections.

The PSF in equation (8) is independent of the incident field amplitude, E_0, and normalized to 1 when integrated over x. Moreover, the computation works at any radiation wavelength, assigning automatically the correct weight to surface diffraction, geometrical optics and scattering. Fig. 3 illustrates this concept: the same profile errors of a couple of mirrors, including low- and high-frequencies, were used to compute [equations (4) and (8)] the PSF expected at three different values of λ. It is clearly seen that the PSF changes from a dominance of the aperture diffraction in UV light to a regime in which low-frequency errors determine it, followed by a rapid increase of the X-ray scattering. We point out that *exactly the same equations* have been used in the three cases, and that the method works very well also with oscillations in the centimetre range (Raimondi & Spiga, 2015).

The explicit computation of equation (8), albeit less efficient than FFT-aided methods, virtually sets no geometrical constraints to the applicability of the simulation (such as distance between subsequent optical elements, angles of incidence, *etc.*). The integration over the transverse direction can be neglected whenever the hypothesis of grazing-incidence angles holds, as in this case the transverse figure error hardly affects the intensity distribution in the focal plane. A generic 2D problem can thus be satisfactorily investigated by slicing the 2D surface into one or many 1D longitudinal

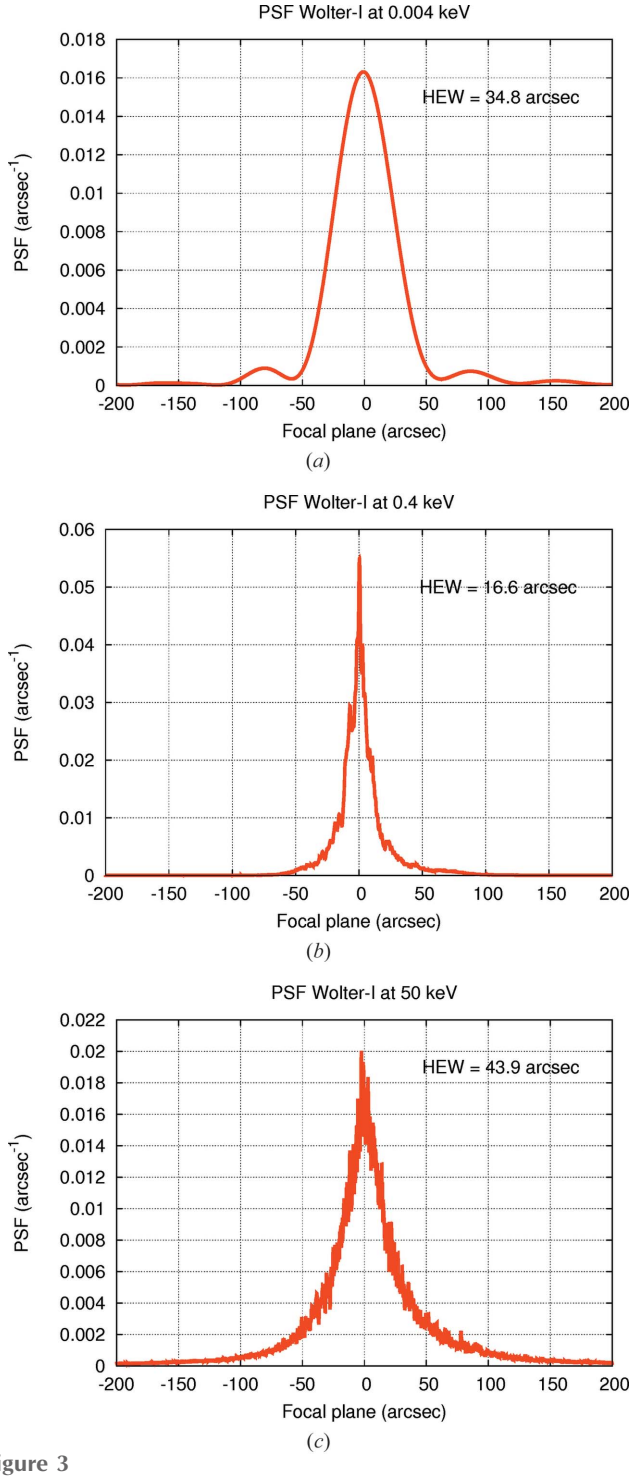

Figure 3
The computed PSF after the propagation through two mirrors at three different energies from a deterministic profile error plus a high-frequency roughness profile (Raimondi & Spiga, 2015). In UV light, the aperture diffraction is the dominant term. At 0.4 keV, the PSF is solely affected by the profile error imparted to the mirror. For hard X-rays, the X-ray scattering from roughness has a major impact on the PSF.

profiles, eventually averaging the intensity distributions. *WISEr* can be fed both with figure error data (typically down to the millimetre scale), expressed as a single height profile or more, and with (micro)-roughness statistics data (typically down to 1 µm), expressed as the power spectral density (PSD) of the microscopic height profiles.

3. KAOS, the KB active optics system

The Kirkpatrick–Baez Active Optics Systems serving DiProI, MagneDyn and LDM endstations at FERMI have been tested and developed continuously between 2012 and 2018 using both FEL1 and FEL2. They consist of thin plane mirrors that are mechanically bent into the desired shape. After several experimental shifts dedicated to the characterization of such systems their performance in terms of spot sizes and shapes have practically reached the nominal opto-mechanical limits. Spots as small as 1.8 µm × 2.4 µm have been obtained, as confirmed by the use of several diagnostic tools such as wavefront sensors, YAG and phosphor screens, and physical ablation on PMMA and silicon substrates. These focusing systems have been successfully used throughout the external users' experiments, and have demonstrated their flexibility in focusing radiation from both the FERMI FEL lines, as well as focusing radiation in experimental chambers mounted behind the endstations of FERMI.

3.1. Mechanical project

Our purpose is the bending of a flat, constant-thickness mirror by the application of unequal end torques in order to obtain a plane-elliptical surface. If the mirror has constant width and thickness, then the result of such bending will be a cubic curve that can be made to approximate an ellipse up to the third order [see equation (10)]. This enables the correction of defocus and coma while leaving higher-order aberrations uncorrected. Higher-order corrections to the bent shape are made, if required, by applying a controlled variation to the mirror width. An elliptical cylindrical mirror is defined by the optical parameters r, r' and θ and has major and minor semi-axes a and b and eccentricity e. It is represented in the XY coordinate system by

$$y = \frac{x^2}{a^2} + \frac{y^2}{b^2} = 1. \tag{9}$$

The same ellipse can also be represented by a power series in the x,y coordinates as

$$y = a_2x^2 + a_3x^3 + a4x^4 + \ldots \tag{10}$$

so that the slope and curvature are

$$\frac{\mathrm{d}y}{\mathrm{d}x} = 2a_2x + 3a_3x^2 + 4a4x^3 + \ldots, \tag{11}$$

$$\frac{\mathrm{d}^2y}{\mathrm{d}^2x} = 2a_2 + 6a_3x + 12a4x^2 + \ldots. \tag{12}$$

Each term a_ix of the series in equation (10) corresponds to an aberration of the reflected wavefront that will be corrected if the term is faithfully built into the mirror shape. The $i = 2$ term corresponds to defocus, the $i = 3$ term to coma [linear variation of curvature with position in the aperture, see equations (11) and (12)], the $i = 4$ term to spherical aberration, and so on

(Howells *et al.*, 2000). Considering, first, a substrate bent by the action of two end torques $C1$ and $C2$, one can show that the bending moment will vary linearly from $C1$ at $X = -L/2$ to $C2$ at $X = +L/2$. The differential equation for the shape of the bent beam is the Bernouilli–Euler equation taking the following form,

$$EI_0 \frac{d^2y}{d^2x} = \frac{C_1 + C_2}{2} - \frac{C_1 - C_2}{L} x, \tag{13}$$

where E is Young's modulus and I_0 is the moment of inertia of the beam cross section, considered constant for our purposes. In order to approximate an ellipse with a third-order expansion, we equate coefficients of $i = 2$ and $i = 3$ to determine the required values of $C1$ and $C2$,

$$\frac{C_1 + C_2}{2} = 2EI_0 a_2 = \frac{EI_0}{R_0}, \tag{14}$$

$$\frac{C_1 - C_2}{L} = -6EI_0 a_3 = -\frac{3EI_0}{R_0} \frac{\sin\theta}{2} \left(\frac{1}{r'} - \frac{1}{r}\right), \tag{15}$$

where R_0 is the radius of curvature at the center. Thus the mirror will match the ellipse up to the third order if the bending moment is equal to $C1$ and $C2$ at $-L/2$ and $+L/2$. There is no need to apply the bending torques exactly at $-L/2$ and $+L/2$ and in fact they are best placed somewhat further from the mirror center to compensate for end-errors.

The solution we developed for our KB mechanical holder is based on the leaf-spring bending mechanisms presented by Howells *et al.* (2000). A sketch of such a system is shown Fig. 4.

In our system the two bending moments $C1$ and $C2$ are applied at $-L/2$ and $+L/2$ making use of external clamps, as shown in Fig. 5(*b*). The last upgraded mechanical holder, which works with improved stability and repeatability, is more effective in preventing the twisting effect and reduces the pressure on the mirror along the longitudinal direction with respect to the initial project (Cocco *et al.*, 2010; Zangrando *et al.*, 2011; Raimondi *et al.*, 2013). In addition, we have also adopted encoders for the motor position and piezo actuators mounted on the clamps to fine tune the curvature. The ellipse sagittas requested for our system amount to about 250 µm for the vertical mirror and about 360 µm for the horizontal mirror.

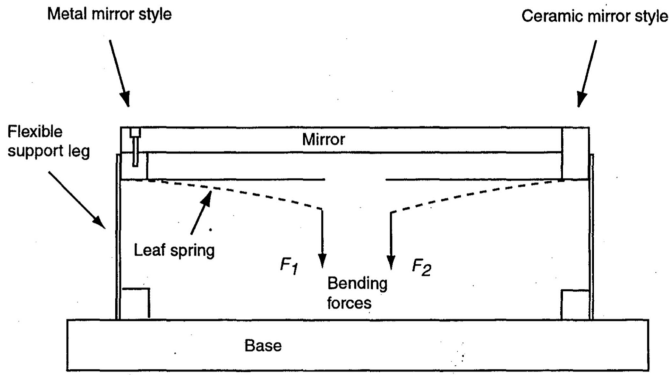

Figure 4
Sketch of leaf-spring bending mechanisms without the tensile force, which does not introduce tension in the mirror (Howells *et al.*, 2000).

The dimensions of the substrate are 400 × 40 × 10 mm, and the mirrors work in grazing incidence at $\theta_i = 2°$. In order to further improve the performance of the system to obtain a nominally exact elliptical shape, we could modify the width of the mirror. According to Howells *et al.* (2000), in this option I_0 in equation (13) becomes $I(x)$ and it is calculated to give the correct radius of curvature at each value of x as specified by equation (13). It is possible to do this for almost any pair of end couples but as an example we use the ones given by equations (14) and (15). Inserting equations (12), (14) and (15) into (13) and remembering that $I = bh^3/12$ where b and h are the width and thickness of the mirror, respectively, we obtain an expression for the width needed to produce the desired elliptical shape,

$$b(x) = \frac{b_0\left[(1/R_0) + 6a_3x\right]}{2a_2 + 6a_3x + 12a_4x^2 + \ldots}. \tag{16}$$

In the case of the FERMI machine that works in the ultraviolet soft X-ray energy range, it should be interesting going further in improving the optical system trying to extend the optimization of the curvature above the third order, modifying the substrate to have variable width or thickness, and adopting piezo actuators behind the mirror substrate. This will be the

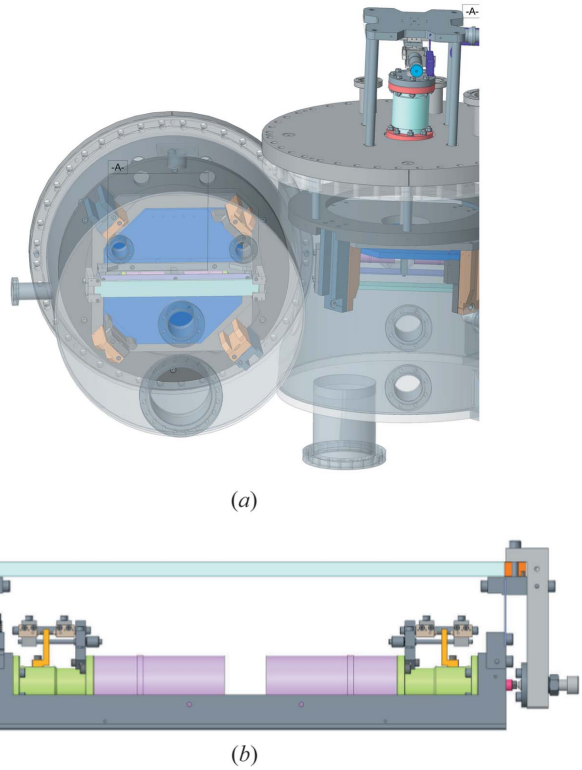

(*a*)

(*b*)

Figure 5
(*a*) Sketch of a Kirkpatrick–Baez vacuum chamber accommodating two holders. The system consists of two elliptical mirrors, focusing the source at a finite distance separately in the vertical and horizontal directions. The source is located at the first focus of each ellipse, while the focal plane is at the second focus. The demagnification is given by the ratio between the mirror–source and mirror–focal-plane distances. (*b*) Mirrors and holders as mounted in the KB vacuum chamber. In the bottom side the two pusher motors bending the mirror are shown.

next step in the development of a new, even better performing, version of the KAOS system.

3.2. Metrology characterization

We characterized the two KB mirrors with a long trace profiler (LTP) at the Optical Metrology Laboratory of Elettra – Sincrotrone Trieste (Sostero *et al.*, 2005). The mechanical system has been optimized with *Adaptive Correction Tool* software (*ACT*) (Signorato, 1998). The software helps in bending the mirrors to profiles as close as possible to the nominal ellipses, *i.e.* with sagittas of 320 µm and 210 µm for the horizontal and vertical mirrors, respectively. A description of the first basic version of the mechanical system has been given by Cocco *et al.* (2010).

As a first step, the *ACT* software calculates the interaction matrix of the mirror bending using a least-squares approach. This matrix is then used to calculate the steps needed by each motor to shape the mirror as close as possible to the desired profile.

This iterative procedure converges very quickly to reach the needed quasi-elliptical mirror deformation relative to the initial reference shape. When the peak-to-valley of the residual is below 1 µm, we started to use the piezo actuators instead of the motors to bend the mirrors (we adopted piezo PI model P-841.20 which has a linear spatial range of 30 µm, which translates into mirror curvature peak-to-valley of around 30 µm). Both sets of motors (steppers and piezos) are closed-loop controlled by means of suitable encoders. The displacement of the clamps is constituted by composite and independent movements, one following the action of the motors and the other due to the clamp-mounted piezo actuators. The best obtained residuals are shown in Fig. 6. We characterized the microroughness with a ZYGO white-light interferometer. The results came in at under 3 Å. Fig. 7 shows the PSD of the microroughness superimposed by a fit with a power-law function of the vertical mirror.

Spiga (2007) derived the equation that computes the contribution of the scattering from microroughness (in terms of PSD) to the PSF degradation in terms of half energy width (HEW) of the spot. If $\mathrm{PSD}(f) \simeq K_n f^{-n}$, the PSD of the microroughness can be fitted by a power law. Then, the expression of the angular spot size in terms of HEW as a function of the wavelength is

$$\mathrm{H}(\lambda) \simeq \left(\frac{K_n}{n-1}\right)^{1/(n-1)} \left(\frac{\sin\theta_\mathrm{i}}{\lambda}\right)^{(3-n)/(n-1)}, \qquad (17)$$

where K_n and n are the power-law parameters, θ_i is the incident angle and λ is the wavelength. Fig. 8 shows the behavior of the HEW contribution of our PSD in micrometres for our KB system with energy in keV. In particular, we considered the worst case, *i.e.* the KB vertical mirror which has the longest focal length. In the FERMI energy range, the scattering contribution appears negligible, less than 0.026 µm, in the worst case at shorter wavelength. This result is in agreement

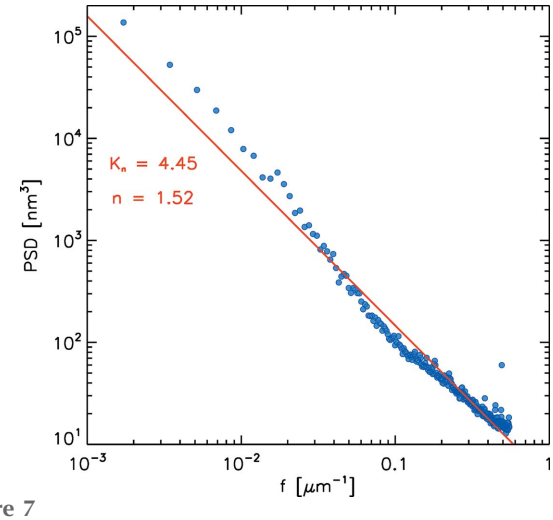

Figure 7
Characterization of the horizontal mirror with the ZYGO white-light interferometer. This picture shows the power spectral density of the microroughness in the spatial range between 1 mm and 1.5 µm of the vertical mirror. The red line represents the best fit obtained with a power-law curve $\mathrm{PSD}(f) \simeq K_n f^{-n}$.

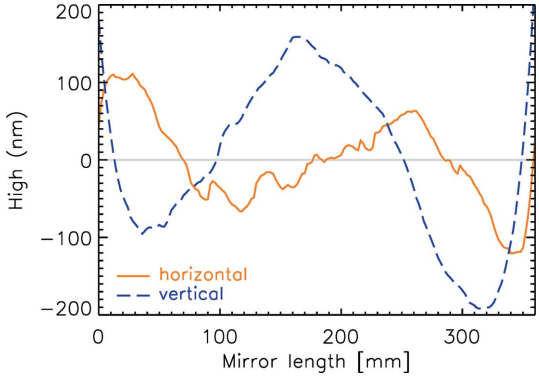

Figure 6
Characterization of the two mirrors with the LTP. The residual surface profiles obtained by subtracting the two ideal ellipses from mirror measured profiles (relative to the horizontal and vertical mirrors) are shown, in the case of focal lengths 1750 mm and 1200 mm in the vertical and horizontal directions, respectively.

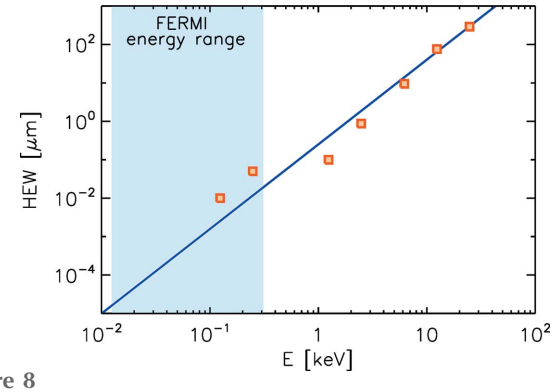

Figure 8
Behavior of the HEW contribution of the measured PSD in terms of scattering effect, converted for our KB system, with the energy in keV (blue line), for the KB vertical mirror with the longest focal length. The red squares represent the values obtained from *WISEr* simulations of the sole roughness. The light blue area represent the FERMI energy range.

with simulations performed with *WISEr* of the sole micro-roughness, ignoring the figure errors.

4. KAOS on DiProI endstation

The DiProI beamline exploits the expected performance of the fully coherent seeded FEL in terms of continuous tunability, with wavelengths between 60 and 4 nm in the first harmonics and temporal pulse duration down to a few tens of femtoseconds at 50 Hz repetition rate, with 10^{13} photons per pulse and variable photon polarization. The beamline is designed to meet the requirements for static and dynamic coherent diffraction imaging (CDI) experiments with a resolution down to 10 nm, while implementing options for complementary projection imaging. The KAOS system is adopted as refocusing optics, and is crucial for imaging single small objects, providing a minimum spot size of 1.8 µm × 2.4 µm and a maximum fluence reaching 1×10^{17} W cm^{-2} at 20 nm wavelength. The beam can be defocused, preserving the spot position, to provide variable spot shape and dimension in order to illuminate larger specimen portions or reduce the fluence.

We performed a set of measurements on the DiProI endstation using a Hartmann sensor from Imagine Optic in order to optimize the KB system in terms of mirror bending and alignment angle. The instrument is mounted out of focus, about 1.5 m behind the DiProI endstation, in order to have a beam dimension comparable with the size of the instrument grid (around 13 mm × 13 mm). The Hartmann sensor software outputs the intensity distribution of the beam, typically a mix between several modes resulting in a 'noisy hyper-Gaussian' intensity profile, and the wavefront residuals from ideal propagation shape corrected for the tilt of the pinhole array plate (see Fig. 9). Combining these two measurements the electric field of the wave at the position of the grid can be obtained (sampled with a number of points equal to the number of pinholes in the array plate). Propagating back the electric field to the focal plane of the KB system, the focal spot can be reconstructed using the far-field approximation.

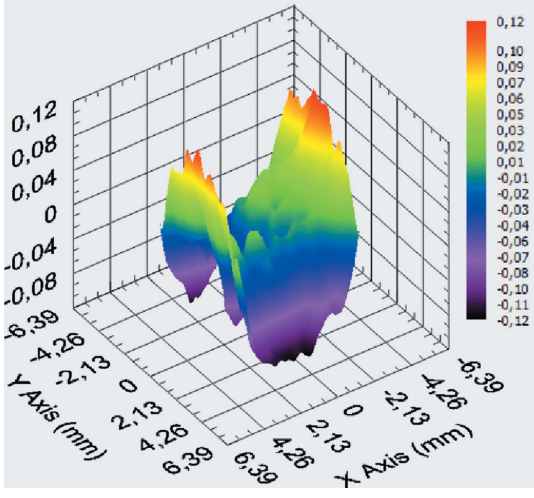

Figure 9
Residual of the wavefront after an optics optimization at 20 nm wavelength. The surface is quite flat with r.m.s. = 0.051 units of λ.

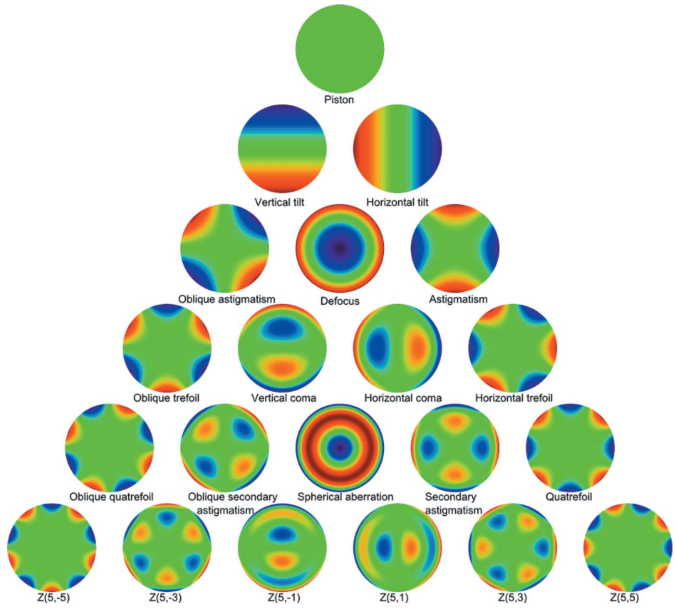

Figure 10
The first 21 Zernike polynomials, ordered vertically by radial inclination and horizontally by azimuth.

In order to optimize the mirror bending, we tried to minimize the aberrations that were quantified in terms of Zernike coefficients (see below), operating on the bendable system parameters which are pitch, roll and bending of each mirror. To ease the interpretation of the wavefront deformation, it is convenient to express wavefront data as an expansion using Zernike polynomials,

$$\begin{aligned} W(\rho,\theta') = {} & Z_0 + Z_1\rho\cos\theta' + Z_2\rho\sin\theta' + Z_3(2\rho^2-1) \\ & + Z_4\rho^2\cos 2\theta' + Z_5\rho^2\sin 2\theta' \\ & + Z_6(3\rho^2-2)\rho\cos\theta' + Z_7(3\rho^2-2)\rho\sin\theta' \\ & + Z_8(6\rho^4-6\rho^2+1)\ldots + \ldots . \end{aligned} \tag{18}$$

The measured wavefront can be decomposed into a linear combination of Zernike polynomials that describe typical optical properties and errors of the optical system, such as defocus, coma, astigmatism and so on (see Fig. 10). The polynomial decomposition gives a numerical representation of any kind of aberration of the sample. In our case, in particular, we considered only the third order of the Zernike parameters because of the limits given by the substrate geometry (see Section 3.1).

The optimal results, both for FEL1 and FEL2, were achieved after several optimization iterations. The left-hand side of Fig. 11 shows the best focal spot achieved at 32 nm with FEL1: 5.5 µm × 6.2 µm [full width at half-maximum (FWHM)]; this value was also confirmed by PMMA ablation imprint measurements seen on the right-hand side of Fig. 11. The left-hand side of Fig. 12 shows the best focal spot achieved at 4.14 nm with FEL2: 1.8 µm × 2.4 µm (FWHM); this value was also confirmed by PMMA ablation imprint measurements

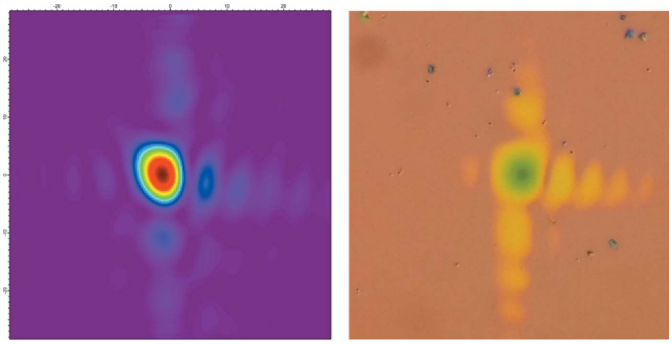

Figure 11
KB system spot size determination by means of different techniques, at 32 nm wavelength with FEL1. Left: reconstructed spot from wavefront sensor data, 5.5 µm × 6.2 µm (FWHM). Right: PMMA-indentation post-mortem analysis of a focal spot created by KB system, estimation size 6 µm × 7 µm (FWHM).

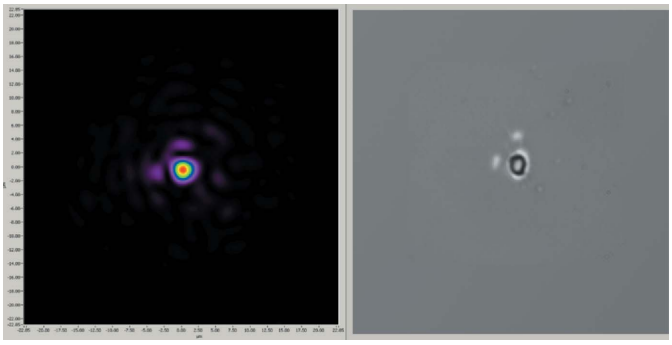

Figure 12
KB system spot size determination by means of different techniques, at 4.14 nm wavelength with FEL2. Left: reconstructed spot from wavefront sensor data, 1.8 µm × 2.4 µm (FWHM). Right: PMMA-indentation post-mortem analysis of a focal spot created by KB system, estimation size 2.0 µm × 2.5 µm (FWHM).

seen on the right-hand side of Fig. 12, that returned 2 µm × 2.4 µm. Moreover, it is worth mentioning that the WFS-based spot determination was recently confirmed also by means of another technique involving an *in situ* fluence-mapping approach. Using a tailored, continuously varying grating underneath the sample, it was possible to further demonstrate the reliability of the wavefront sensor as a spot-determining technique (Schneider *et al.*, 2018).

4.1. *WISEr* simulations

DiProI was also simulated using *WISEr*, taking into account the plane mirrors along the FERMI photon transport, and the KB active system. For KAOS we considered the best figure errors achieved shown in Fig. 6, and the microroughness profiles given by the measured PSDs seen in Fig. 7. The simulations have been performed at a wavelength of 4.14 nm for FEL2, and 32 nm and 60 nm for FEL1. We considered three plane mirrors in the horizontal direction (the non-invasive spectrometer is considered as a plane mirror as it works at zero order) and one in the vertical direction for FEL1 (see Fig. 1). In the case of FEL2 we have one less plane mirror (PM1b) in the horizontal direction.

Fig. 13 shows the results of the simulations of the KB mirror focal spots at best focus in the DiProI chamber at 32 and 60 nm wavelength for FEL1, and at 4.14 nm wavelength for FEL2. We performed these simulations making use of the *WISEr* simulation tool, considering all mirrors of the beamline and theirs defects, in terms of figure errors and microroughness. The microroughness profiles are obtained from the measured PSD, and for a more correct statistical approach we averaged simulations from the same figure errors but different roughness profile given by the same PSD. The results are as follows: at 4.14 nm wavelength with FEL2, 1.7 µm × 2.2 µm (FWHM); at 32 nm wavelength with FEL1, 5.1 µm × 6.0 µm (FWHM); at 60 nm wavelength with FEL1, 8.6 µm × 11.2 µm (FWHM). Since we obtained the residual of the KB *ex situ* using the LTP and with the help of the *ACT* software, we have to consider these results as the limits of the mechanical system. For this reason, we have to assume the results returned by *WISEr* as the best we could achieve with the optimization and alignment of the system during the experiment preparation on

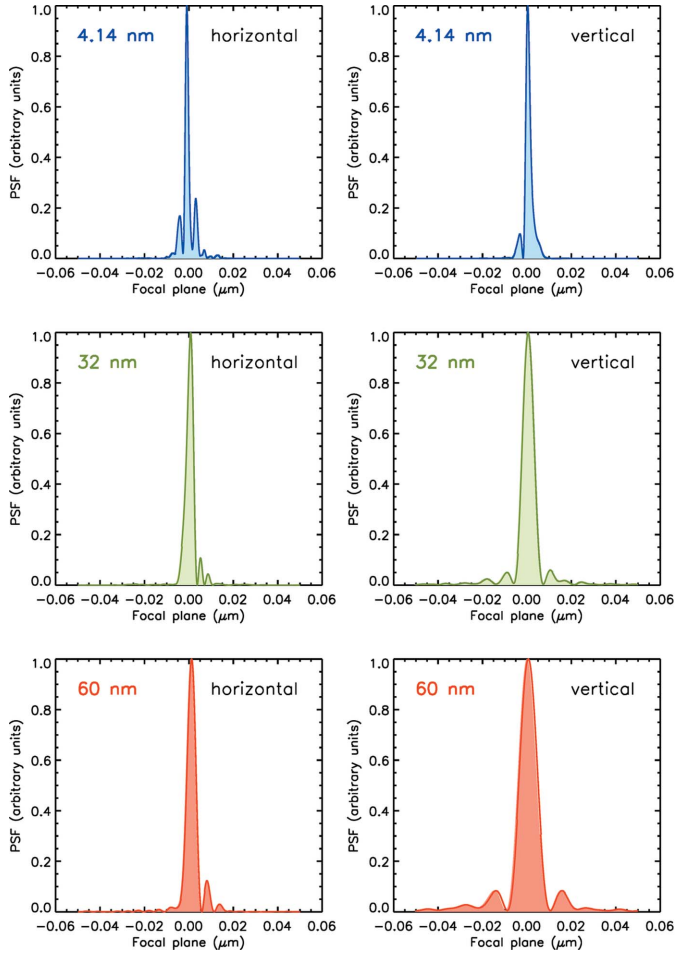

Figure 13
Simulations performed with *WISEr* of the KB system focal spot, taking into account figure errors and microroughness of all mirrors. Top panels show simulation at 4.14 nm with FEL2, resulting in 1.7 µm × 2.2 µm (FWHM). Middle panels refer to 32 nm with FEL1 (5.1 µm × 6.0 µm FWHM) and bottom panels refer to 60 nm with FEL1 (8.6 µm × 11.2 µm FWHM).

the DiProI endstation. Comparing the simulation in Fig. 13, and the focal spot obtained on DiProI seen in Figs. 11 and 12, we can conclude that, by using a wavefront sensor as diagnostic of the focal spot and to optimize the KB active optics system alignment, it is possible to approach the limits of the optical system.

4.2. Impact of different spatial wavelengths on the spot size

The purpose of the study presented in this section is to understand how to further improve our KB system performance. Here, to quantify the quality of the focal spot we used the HEW instead of the FWHM. The HEW is defined as the diameter that contains the half integral of the spot intensity. We analyzed the impact of different spatial wavelengths on the PSF degradation. Fig. 14 shows the behavior of the HEW, simulated at different energies, 60 nm, 32 nm and 4.14 nm, filtering the spatial wavelengths using *WISEr*. We considered the case of the KB system of the DiProI endstation taking into account the mirror profiles measured with the LTP previously shown in Fig. 6, and the PSD of the microroughness shown in Fig. 7. In particular, we considered the horizontal mirror. We subtracted the harmonics from the profiles, applying a low-pass filter in wavelengths before computing the HEW simulations using *WISEr*. The HEW thereby becomes a function of the low-pass wavelength, and in general an increasing one. Likewise, we are able to determine the spatial wavelength with the largest impact on the HEW degradation. The left-hand side of the plot represents the ideal elliptical profile. The HEW is determined only by aperture diffraction and by the demagnification of the optical system. Moving towards the right-hand side of the plot, we added longer and longer spatial wavelengths until we reconstructed the complete measured profile of the mirror.

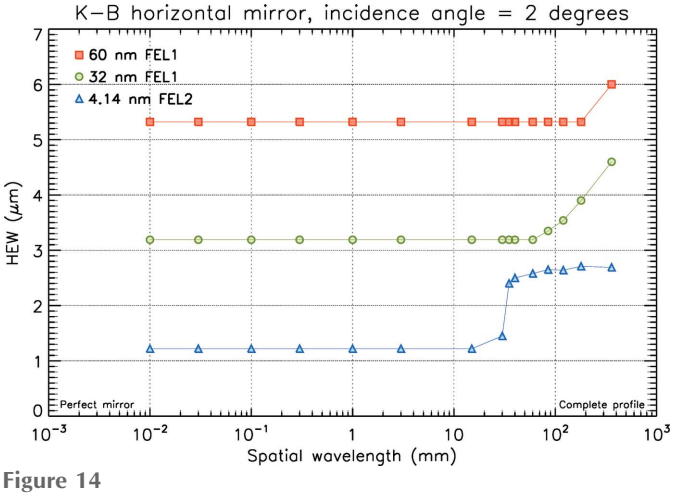

Figure 14
The behavior of the HEW filtering the spatial wavelength of the profile in the case of the DiProI KB system vertical mirror. The left-hand side of each graph represents a situation close to an *ideal* elliptic profile, so the HEW becomes almost constant and determined only by the diffraction limit and by the demagnification of the optical system. Moving to the right, we add longer and longer spatial wavelengths until we reconstruct the fully measured profile of the mirror at the right side. Notice the plateau above 40 mm in the case of 4.14 nm beam wavelength; this is probably due to the non-isotropic nature of the FEL emission.

We started from a perfect mirror and then added surface defect components, going from the high frequencies (*i.e.* short spatial wavelengths) to the lower frequencies (up to the one with a period equal to the length of the mirror), until the profile is complete (the right-hand side of the plot). For every profile, the PSF and the HEW were estimated. Fig. 14 shows, for the KB horizontal mirror, the behavior of the HEW with the spatial wavelength cutoff. The 4.14 nm case shows a plateau at longer spatial wavelengths (above 40 mm), where the HEW stops increasing. This is probably due to the non-isotropic nature of the FEL emission, that is Gaussian-like with energy-dependent divergence. In fact, the higher the photon energy, the smaller the divergence, so the beam interacts differently with long spatial wavelengths whenever the beam projection size become smaller than the mirror length. The footprint of the beam at 4.14 nm is around 35 mm, exactly the same dimension where the plateau starts. Note that the HEW begins to increase in correspondence to a particular value of the spatial wavelength that depends on the incident wavelength. Additionally, the higher the energy, the shorter the corresponding spatial wavelength cutoff. In the three cases considered (60 nm and 32 nm for FEL1, 4.14 nm for FEL2), we have found that the approximate turning points are 120 mm, 60 mm and 12 mm, respectively. This means that the focal spot degradation is due to long spatial wavelengths, longer than 12 mm. Furthermore, the strong impact of the spatial wavelength 32.8 mm to the HEW degradation at 4.14 nm is evident. If we want to further improve this system we have to improve the profile in the long spatial wavelength regime, that is, trying different plane mirror substrate shapes, as shown in Section 3.1 (Rah *et al.*, 1997; Eng *et al.*, 1998; Howells *et al.*, 2000).

5. Conclusions

In this work the KB Active Optics System operating on some of the FERMI FEL beamlines has been presented. The system, after a mechanical upgrade discussed in the present work, is now capable of producing focal spot sizes as low as 1.8 μm × 2.4 μm, with aberration correction and alignment optimization powered by wavefront sensing techniques. The results were discussed in terms of physical optics simulations whose results are in very good agreement with spot sizes and shapes obtained by different diagnostical techniques. The *WISEr* simulation code, moreover, was also used to determine the influence of different spatial wavelengths on the PSF degradation, leading to possible strategies to further improve the focusing, *e.g.* adopting substrates with variable thickness or lateral shape, in order to correct orders higher than the third. Nonetheless, the present capabilites of KAOS are already state-of-the-art and they are heavily and proficuously employed in the experiments carried out at FERMI.

Acknowledgements

The authors acknowledge the support received from the whole FERMI Team who have supported all the experiments.

Funding information

This work was funded by the FERMI project of Elettra-Sincrotrone Trieste, partially supported by the Ministry of University and Research under Grant Nos. FIRB-RBAP045JF2 and FIRB-RBAP06AWK3.

References

Allaria, E., Appio, R., Badano, L., Barletta, W. A., Bassanese, S., Biedron, S. G., Borga, A., Busetto, E., Castronovo, D., Cinquegrana, P., Cleva, S., Cocco, D., Cornacchia, M., Craievich, P., Cudin, I., D'Auria, G., Dal Forno, M., Danailov, M. B., De Monte, R., De Ninno, G., Delgiusto, P., Demidovich, A., Di Mitri, S., Diviacco, B., Fabris, A., Fabris, R., Fawley, W., Ferianis, M., Ferrari, E., Ferry, S., Froehlich, L., Furlan, P., Gaio, G., Gelmetti, F., Giannessi, L., Giannini, M., Gobessi, R., Ivanov, R., Karantzoulis, E., Lonza, M., Lutman, A., Mahieu, B., Milloch, M., Milton, S. V., Musardo, M., Nikolov, I., Noe, S., Parmigiani, F., Penco, G., Petronio, M., Pivetta, L., Predonzani, M., Rossi, F., Rumiz, L., Salom, A., Scafuri, C., Serpico, C., Sigalotti, P., Spampinati, S., Spezzani, C., Svandrlik, M., Svetina, C., Tazzari, S., Trovo, M., Umer, R., Vascotto, A., Veronese, M., Visintini, R., Zaccaria, M., Zangrando, D. & Zangrando, M. (2012). *Nat. Photon.* **6**, 699–704.

Allaria, E., Bencivenga, F., Borghes, R., Capotondi, F., Castronovo, D., Charalambous, P., Cinquegrana, P., Danailov, M. B., De Ninno, G., Demidovich, A., Di Mitri, S., Diviacco, B., Fausti, D., Fawley, W. M., Ferrari, E., Froehlich, L., Gauthier, D., Gessini, A., Giannessi, L., Ivanov, R., Kiskinova, M., Kurdi, G., Mahieu, B., Mahne, N., Nikolov, I., Masciovecchio, C., Pedersoli, E., Penco, G., Raimondi, L., Serpico, C., Sigalotti, P., Spampinati, S., Spezzani, C., Svetina, C., Trovò, M. & Zangrando, M. (2013). *Nat. Commun.* **4**, 2476.

Allaria, E., Callegari, C., Cocco, D., Fawley, W. M., Kiskinova, M., Masciovecchio, C. & Parmigiani, F. (2010). *New J. Phys.* **12**, 075002.

Capotondi, F., Pedersoli, E., Bencivenga, F., Manfredda, M., Mahne, N., Raimondi, L., Svetina, C., Zangrando, M., Demidovich, A., Nikolov, I., Danailov, M., Masciovecchio, C. & Kiskinova, M. (2015). *J. Synchrotron Rad.* **22**, 544–552.

Church, E. L. (1979). *Proc. SPIE*, **0184**, 196–202.

Cocco, D., Bortoletto, G., Sergo, R., Sostero, G. & Cudin, I. (2010). *Nucl. Instrum. Methods Phys. Res. A*, **616**, 128–133.

di Cicco, A., Bencivenga, F., Battistoni, A., Cocco, D., Cucini, R., D'Amico, F., di Fonzo, S., Filipponi, A., Gessini, A., Giangrisostomi, E., Gunnella, R., Masciovecchio, C., Principi, E. & Svetina, C. (2011). *Proc. SPIE*, **8077**, 807704.

Eng, P. J., Newville, M., Rivers, M. L. & Sutton, S. R. (1998). *Proc. SPIE*, **3449**, 145–156.

Foglia, L., Bencivenga, F., Mincigrucci, R., Simoncig, A., Calvi, A., Cucini, R., Principi, E., Zangrando, M., Mahne, N., Manfredda, M., Raimondi, L., Pedersoli, E., Capotondi, F., Kiskinova, M. & Masciovecchio, C. (2017). *Proc. SPIE*, **10237**, 102370C.

Howells, M. R., Cambie, D., Irick, S. C., MacDowell, A. A., Padmore, H. A., Renner, T. R., Rah, S. Y. & Sandler, R. (2000). *Opt. Eng.* **39**, 2748–2762.

Kirkpatrick, P. & Baez, A. V. (1948). *J. Opt. Soc. Am.* **38**, 766–774.

Masciovecchio, C., Battistoni, A., Giangrisostomi, E., Bencivenga, F., Principi, E., Mincigrucci, R., Cucini, R., Gessini, A., D'Amico, F., Borghes, R., Prica, M., Chenda, V., Scarcia, M., Gaio, G., Kurdi, G., Demidovich, A., Danailov, M. B., Di Cicco, A., Filipponi, A., Gunnella, R., Hatada, K., Mahne, N., Raimondi, L., Svetina, C., Godnig, R., Abrami, A. & Zangrando, M. (2015). *J. Synchrotron Rad.* **22**, 553–564.

O'Keeffe, P., Bolognesi, P., Richter, R., Moise, A., Ovcharenko, Y., King, G. C. & Avaldi, L. (2011). *Phys. Rev. A*, **84**, 025404.

Pedersoli, E., Capotondi, F., Cocco, D., Zangrando, M., Kaulich, B., Menk, R. H., Locatelli, A., Mentes, T. O., Spezzani, C., Sandrin, G., Bacescu, D. M., Kiskinova, M., Bajt, S., Barthelmess, M., Barty, A., Schulz, J., Gumprecht, L., Chapman, H. N., Nelson, A. J., Frank, M., Pivovaroff, M. J., Woods, B. W., Bogan, M. J. & Hajdu, J. (2011). *Rev. Sci. Instrum.* **82**, 043711.

Prince, K. C., Allaria, E., Callegari, C., Cucini, R., De Ninno, G., Di Mitri, S., Diviacco, B., Ferrari, E., Finetti, P., Gauthier, D., Giannessi, L., Mahne, N., Penco, G., Plekan, O., Raimondi, L., Rebernik, P., Roussel, E., Svetina, C., Trovò, M., Zangrando, M., Negro, M., Carpeggiani, P., Reduzzi, M., Sansone, G., Grum-Grzhimailo, A. N., Gryzlova, E. V., Strakhova, S. I., Bartschat, K., Douguet, N., Venzke, J., Iablonskyi, D., Kumagai, Y., Takanashi, T., Ueda, K., Fischer, A., Coreno, M., Stienkemeier, F., Ovcharenko, Y., Mazza, T. & Meyer, M. (2016). *Nat. Photon.* **10**, 176–179.

Rah, S. Y., Locklin, S. C., Irick, S. C. & Howells, M. R. (1997). *Proc. SPIE*, **3152**, 112–119.

Raimondi, L. & Spiga, D. (2010). *Proc. SPIE*, **7732**, 77322Q.

Raimondi, L. & Spiga, D. (2015). *Astron. Astrophys.* **573**, A22.

Raimondi, L., Svetina, C., Mahne, N., Cocco, D., Abrami, A., De Marco, M., Fava, C., Gerusina, S., Gobessi, R., Capotondi, F., Pedersoli, E., Kiskinova, M., De Ninno, G., Zeitoun, P., Dovillaire, G., Lambert, G., Boutu, W., Merdji, H., Gonzalez, A. I., Gauthier, D. & Zangrando, M. (2013). *Nucl. Instrum. Methods Phys. Res. A*, **710**, 131–138.

Sanchez del Rio, M., Rebuffi, L., Demsar, J., Canestrari, N. & Chubar, O. (2014). *Proc. SPIE*, **9209**, 92090X.

Schneider, M., Günther, C. M., Pfau, B., Capotondi, F., Manfredda, M., Zangrando, M., Mahne, N., Raimondi, L., Pedersoli, E., Naumenko, D. & Eisebitt, S. (2018). *Nat. Commun.* **9**, 214.

Signorato, R. (1998). *Proc. SPIE*, **3447**, 20–31.

Sostero, G., Cocco, D. & Bianco, A. (2005). *Proc. SPIE*, **5921**, 89–97.

Spiga, D. (2007). *Astron. Astrophys.* **468**, 775–784.

Stover, J. C. (1995). *Optical Scattering. Measurement and Analysis.* SPIE Optical Engineering Press.

Svetina, C., Dell'Angela, M., Mahne, N., Malvestuto, M., Parmigiani, F., Raimondi, L. & Zangrando, M. (2014). *Proc. SPIE*, **9207**, 92070E.

Svetina, C., Grazioli, C., Mahne, N., Raimondi, L., Fava, C., Zangrando, M., Gerusina, S., Alagia, M., Avaldi, L., Cautero, G., de Simone, M., Devetta, M., Di Fraia, M., Drabbels, M., Feyer, V., Finetti, P., Katzy, R., Kivimäki, A., Lyamayev, V., Mazza, T., Moise, A., Möller, T., O'Keeffe, P., Ovcharenko, Y., Piseri, P., Plekan, O., Prince, K. C., Sergo, R., Stienkemeier, F., Stranges, S., Coreno, M. & Callegari, C. (2015). *J. Synchrotron Rad.* **22**, 538–543.

Zangrando, M., Cocco, D., Fava, C., Gerusina, S., Gobessi, R., Mahne, N., Mazzucco, E., Raimondi, L., Rumiz, L. & Svetina, C. (2015). *J. Synchrotron Rad.* **22**, 565–570.

Zangrando, M., Cudin, I., Fava, C., Gerusina, S., Gobessi, R., Godnig, R., Rumiz, L., Svetina, C., Parmigiani, F. & Cocco, D. (2011). *Proc. SPIE*, **8078**, 80780I.